Effects of confining pressure on the permeability of three rock types under compression

A.K.M. Badrul ALAM[1], Masaki NIIOKA[1], Yoshiaki FUJII[1], Daisuke FUKUDA[1] and Jun−ichi KODAMA[1]

[1] Rock Mechanics Laboratory, Graduate School of Engineering, Hokkaido University, Kita 13 Nishi 8, Kita−ku, Sapporo, Hokkaido 060−8628, Japan

*Corresponding author: A.K.M. Badrul ALAM
E−mail: badrul@ eng.hokudai.ac.jp
TEL&FAX: +81−11−706−6302

ABSTRACT

Triaxial tests were conducted under confining pressures of 1–15 MPa at 295 K using an ultra-compact triaxial cell. The samples were held for 24 h under the target consolidation pressure, and then constant strain-rate compression was applied measuring permeability. The structural changes were measured by thin section image analysis and micro-focus X-ray computed tomography. For the Shikotsu welded tuff, the permeability decreased monotonously with axial compression. The decrease ratio of permeability increased with confining pressure mainly due to pore collapse. An equation representing the post-compression permeability with confining pressure was proposed. For the Kimachi sandstone, the permeability first decreased with increasing axial stress, then began to increase when the total lateral strain recovered its value before the application of confining pressure, and then maintained an almost constant value in the post-peak region. The minimum and final permeability decreased with increasing confining pressure mainly due to compaction and large plastic deformation of clay cementing materials. The final permeability was larger under small confining pressures and smaller under high confining pressures than the permeability before axial compression. Based on these observations, new equations were proposed representing the minimum and stable permeability and the strain at the permeability values with confining pressure. For the Inada granite, the tendency of permeability change during axial compression was almost the same as for the Kimachi sandstone. A new equation representing the minimum permeability mainly due to elastic deformation as a function of the confining pressure was proposed. The final permeability was larger than that before compression, and the permeability decreased with smaller confining pressure mainly due to a decrease in the number and width of rupture planes and the absence of axial cracks from biotite. The permeability, however, increased under larger confining pressures mainly due to the formation of subrupture planes caused by the high stress concentration at the rough and stiff rupture plane under large confining pressure.

Keywords: Confining pressure; Permeability; Compression; Sealability; EdZ; EDZ

1. Introduction

Excavation disturbed Zone (EdZ) and Excavation Damaged Zone (EDZ) occur at all types of excavation, and stress redistribution and changes in permeability due to the excavations happen within the zones [1-10]. The interaction between these changes, known as hydromechanical (HM) coupling, significantly affects the sealability of these zones and both the short- and long-term stability of excavations for a wide range of applications, including tunneling, coal mining and coal methane extraction, oil and gas extraction, hydrogeological and well test analyses, geothermal energy, deep well injection of liquid and solid wastes, geologic storage of natural gas, and geologic sequestration of CO_2, as well as a variety of geologic processes [11,12].

Many factors affect EDZs. These include excavation methods such as drilling and blasting and mechanical excavation methods, mechanical changes caused by stress redistribution, ventilation, humidity, and long-term chemical and biological effects [10]. Under triaxial compression, EdZs or EDZs can be recognized in an intact saturated rock beneath or near peak stress levels by stress redistribution around the underground excavation (Fig. 1a). The rock can then reach its residual strength state in the course of time (Fig. 1b). As excavations proceed at different depths and in different types of rock, the rock permeability can be changed by confining pressure as HM processes; thus, it is important to evaluate permeability before and within the residual strength state.

The objective of this study was to investigate the confining pressure dependency of the permeability of three types of rock under compression and to clarify the relevant mechanisms. The types of rock considered were Shikotsu welded tuff as an example of a soft pyroclastic rock, Kimachi sandstone as a medium-hard clastic rock, and Inada granite as a hard crystalline rock. Triaxial tests were carried out at confining pressures of 1–15 MPa at 295 K. The samples were held for 24 h at the target consolidation pressure, and then constant strain-rate compression was applied. Permeability was measured by the constant flow or transient pulse method. In addition, X-ray computed tomography (CT) observation and thin-section image analysis were carried out on the specimens after compression. CT images were obtained in three perpendicular planes to determine the macroscopic failure conditions. Microstructure analysis was

conducted using thin-section images of specimens that had been impregnated with blue resin.

A maximum effective confining pressure of 15 MPa was established by the maximum capacity of the apparatus. Although this effective confining pressure may not seem sufficiently high, especially for Inada granite, it corresponds to the effective vertical stress at a depth of 880 m assuming that the vertical stress is equal to the overburden pressure. Because most underground caverns are constructed to depths of less than 1000 m, this maximum confining pressure value is meaningful.

Many studies have been conducted to understand the behavior of permeability under compression. This research, however is unique because (1) the number of tests densely covered the range of confining pressures, (2) axial compression was applied so as to observe the entire permeability–axial strain relationship up to the residual strength, (3) results for three different rock types were compared, and (4) both CT scanning and thin-section analysis were carried out to determine the macroscopic and microscopic structures of the specimens after the experiments. Points (1) and (2), although not applicable for all rocks, enabled us to propose equations to represent the minimum and final permeability with respect to confining pressure. Points (3) and (4) enabled us to describe the different influences of axial compression and confining pressure on permeability based on mechanical properties that differed by origin, mineral composition, and microstructures.

2. Materials and methods

2.1 Specimen and sample preparation

The Shikotsu welded tuff was sampled at Hokkaido, Japan, and consisted of plagioclase, hypersthene, augite, hornblende, and transparent glass having a felt-like structure with amoebic form in the matrix. The grain sizes of the minerals were 0.3–1.5 mm for plagioclase, about 0.5 mm for hypersthene, 0.3–0.7 mm for augite, and 0.5–1.0 mm for hornblende [13]. The Kimachi sandstone was sampled at Shimane, Japan, and was a relatively well-sorted clastic rock with a typical grain size range of 0.4–1.0 mm. It consisted mostly of rock fragments of andesite; crystal fragments of plagioclase, pyroxene, hornblende, biotite, and quartz; calcium carbonate and iron oxides; and matrix zeolites [14]. The Inada granite

was sampled in Ibaraki, Japan. The composition of the rock was mainly quartz, feldspar, biotite, and allanite, with zircon, apatite, and ilmenite as accessory minerals. The grain sizes of the minerals were 3.0–4.0 mm (on average) for quartz, approximately 2.0–3.0 mm for plagioclase, approximately 2.0–4.0 mm for alkali feldspar, and generally less than 1.0 mm for biotite [15]. The physical properties of these rocks are listed in Table 1.

The specimens were prepared from blocks of the three types of rock using the following steps. (1) The P-wave velocity along each pair of opposite sides of the rock blocks was measured with 140-kHz sensors. (2) Cylindrical cores with a diameter of 30 mm and a length of 60 mm were prepared in the direction of the slowest P-wave velocity. (3) The core ends were polished to a parallelism of 2/100.

The samples were prepared using the following procedure. (1) Each specimen was made fully pure-water saturated in a water-submergible vacuum jar. (2) Two stainless steel endpieces were attached to a saturated specimen with vinyl tape. The endpieces had a central hole to allow water flow through the specimen. (3) Two cross-type strain gauges were glued to the center of opposite sides of the specimen. (4) A coating of silicon sealant was applied to maintain the water flow within the specimen up to the curvature of the endpieces. (5) A heat-shrinkable tube was jacketed to the endpieces-attached specimen to prevent direct contact of the confining fluid (water) with the specimen. (6) The sample was then held in water for 24 h.

2.2 Experimental setup (Fig. 2a)

A loading frame was used to apply the axial load. A double ball plunger pump with a relief valve that was connected to the ultra-compact triaxial cell was used to maintain the confining pressure throughout the experiment. A pair of stainless steel attachments was attached to the jacketed sample. Each attachment had a hole for water flow and a pore pressure sensor. In the constant flow method, the water flow path of the upper attachment was open to the atmosphere; a syringe pump was connected to the lower attachment and used to produce a constant flow of water. In the transient pulse method, an accumulator was connected to the upper attachment, which was upstream; the syringe pump was used to maintain the pore pressure and acted as a downstream accumulator (Fig. 2a).

2.3 Experimental procedure

The experimental procedure was as follows. (1) The sample was inserted into the triaxial cell. (2) The upper and lower attachments were attached to the endpieces. (3) Axial stress and confining pressure were applied to the specimen through the triaxial cell. To reach the target consolidation pressure, the axial stress was applied first, and then the confining pressure was increased in 1-MPa steps (Fig. 2d). After reaching the target consolidation pressure and pore pressure (in the transient pulse method), the sample was held in this state for 24 h at 295 K. (4) After consolidation for 24 h, a constant strain rate (10^{-5} s^{-1}, i.e., 0.036 mm/min)-controlled compression was applied until the stroke-based strain reached 10% for the Shikotsu welded tuff or 7% for the Kimachi sandstone and Inada granite. During the experiment, the load, stroke, pore pressure, axial strain, lateral strain, confining pressure, and flow rate were measured at a sampling interval of 10 s.

2.4 Effective confining pressure, differential stress, and strain correction

The effective confining pressure ($P_{\mathrm{c-effective}}$) for the constant flow method was calculated as:

$$P_{\mathrm{c-effective}} = P_{\mathrm{c}} - \frac{P_{\mathrm{pu}}}{2}, \tag{1}$$

where P_{c} is the confining pressure and P_{pu} is the upstream pore pressure. For the transient pulse method, $P_{\mathrm{c-effective}}$ was calculated as:

$$P_{\mathrm{c-effective}} = P_{\mathrm{c}} - P_{\mathrm{p}}. \tag{2}$$

The differential stress (σ_{diff}) was calculated using the following equation:

$$\sigma_{\mathrm{diff}} = \sigma_{\mathrm{axial}} - P_{\mathrm{c}}, \tag{3}$$

where σ_{axial} is the axial stress.

The effective stress coefficient should be less than 1 for usual rocks and sometimes its value more than 1 was reported for clay-rich rocks [16]. It was however assumed as 1 for the above calculations. The assumption did not cause significant errors for the effective stress values since the pore pressure was as large as slightly more than 1 MPa. When testing the Shikotsu welded tuff, the strain gauges were damaged under some relatively high confining pressures because of pores on the rock surface. When testing the other rocks, the strain

gauges were damaged around the peak stress. To obtain the entire stress–strain (ε') and permeability relationship, the strain gauge strain (ε) was used up to 50% of the peak stress, σ_{50}:

$$\varepsilon' = \varepsilon \,, \sigma < \sigma_{50} \tag{4}$$

A correction was made for the stroke-based strain (ε_s):

$$\varepsilon'' = \varepsilon_s - C\sigma \tag{5}$$

$$\varepsilon' = \varepsilon'' - \varepsilon''_{50} + \varepsilon_{50} \,, \sigma \geq \sigma_{50} \tag{6}$$

$$C = \frac{1}{E_{s50}} - \frac{1}{E_{50}} \,, \tag{7}$$

where E_{s50} is the stroke-based 50% tangent modulus, E_{50} is the strain gauge-based 50% tangent modulus, ε''_{50} is ε'' at the 50% stress level, and ε_{50} is ε at the 50% stress level.

2.5 Measurement of permeability

The permeability of the Shikotsu welded tuff was relatively high, and was measured by the constant flow method. In this method, a constant flow (0.3 ml/min) of pure water was maintained in the axial direction by using the syringe pump (Fig. 2b). Based on Darcy's law, the permeability K (m^2) was calculated by

$$K = \frac{q \cdot \mu}{A} \cdot \left(\frac{\mathrm{d}P}{\mathrm{d}L} \right)^{-1} , \tag{8}$$

where q is the flow rate (m^3/s), μ is the fluid viscosity (Pa·s), A is the cross-sectional area (m^2) of the specimen, and dP/dL is the pressure gradient (Pa/m).

The permeability of the Kimachi sandstone and Inada granite was relatively low, and was measured by the transient pulse method. A constant pore pressure of 1 MPa was maintained in the entire system during consolidation and compression. At every permeability measurement point, the platen was stopped. Then, the accumulator and syringe pump were separated by closing the valve, and a 0.5-MPa pore pressure was applied downstream and the syringe pump was stopped. This condition was maintained for 30 min. Considering the upstream and downstream volumes and a pressure pulse based on the Brace principle [17], we can write:

$$P_1 - P_f = \Delta P_0 \cdot \frac{V_2}{V_1 + V_2} \cdot e^{-\alpha t} \tag{9}$$

$$P_2 - P_f = -\Delta P_0 \cdot \frac{V_1}{V_1 + V_2} \cdot e^{-\alpha t} \tag{10}$$

$$\alpha = \frac{KA}{\mu \beta L} \cdot \frac{V_1 + V_2}{V_1 V_2}, \tag{11}$$

where P_1 is the upstream pressure (Pa), V_1 is the upstream volume (m^3), V_2 is the downstream volume (m^3), P_f is the converged pressure value (Pa), ΔP_0 is the pressure pulse (Pa), t is the elapsed time (s), K is the permeability (m^2), A is the sectional area (m^2), L is the length of the specimen (m), μ is the viscosity of water (Pa·s), and β is the compressibility of water (Pa^{-1}). Then, we obtain

$$P_1 - P_2 \equiv \Delta P = \Delta P_0 \cdot e^{-\alpha t} \tag{12}$$

Defining G_1 and G_2 as the upstream and downstream stiffness (Pa/m^3) of the hydraulic system, respectively, the upstream and downstream volumes are expressed as

$$V_i = \frac{1}{\beta G_i}, \quad i = 1, 2 \tag{13}$$

Substituting Eq. (13) into Eq. (11), we obtain the following expression:

$$\alpha = \frac{KA}{\mu L} \cdot (G_1 + G_2) \tag{14}$$

Therefore, the resultant expression for K is

$$K = \frac{\mu L \alpha}{(G_1 + G_2) A} \tag{15}$$

After obtaining the gradient α (s^{-1}) from the time−lnΔP curve (Fig. 2c), the permeability was calculated from Eq. (15).

2.6 Micro- and macrostructure analysis

Microstructure analysis was conducted from thin-section images of the blue resin-impregnated specimens using Scion Image software [18] with a resolution of 8.8 μm. A micro-focus X-ray computed tomography (CT) scanner, installed at Hokkaido University, Japan, was also used to determine the number, orientation, and geometry of the rupture planes (i.e., the post-compression macrostructure of the specimens). A detailed description of micro-focus X-ray CT for rock-like materials is provided in Fukuda et al. [19]. The CT images were obtained in three perpendicular planes with a resolution of 37 μm.

3. Results of the Shikotsu welded tuff

3.1 Deformation and permeability

This rock exhibited strain softening at a confining pressure (P_c) of 1 MPa, almost perfect plastic behavior at P_c = 5 MPa, and strain hardening at P_c = 10 and 15 MPa (Fig. 3a). The peak differential stress increased up to P_c = 5 MPa (Fig. 3b). At P_c > 10 MPa, i.e., strain hardening, the yield stress decreased slightly with increasing confining pressureand the residual strength increased with the confining pressure(Fig. 3b), but no clear relationship was observed for the tangent modulus or Poisson's ratio (Fig. 3c).

The permeability was lowest at a confining pressure of 15 MPa, compared to P_c = 1–10 MPa, after 24 h of consolidation (Fig. 4a). The permeability did not decrease significantly at P_c = 1 MPa, showed a significant decrease after the peak load at P_c = 5–10 MPa, and decreased monotonously at P_c = 15 MPa due to axial compression (Fig. 3a).

The permeability change was calculated from the permeability after consolidation (K_{con}) and the permeability after compression (K_{com}):

$$K_{change} = \frac{K_{com} - K_{con}}{K_{con}} \times 100 \tag{16}$$

The permeability decrease was small at P_c = 1 MPa, but the amount of the decrease became larger with increasing confining pressure (Fig. 4c). The relationship between permeability (m^2) after compression and confining pressure, P_c (MPa), can be approximated by the following equation:

$$\log K_{com} = -14.37 - 0.61 \log P_c \tag{17}$$

3.2 Micro- and macrostructures

Microstructure analysis was conducted using the blue resin-impregnated thin-section images. The thin section of the 15-MPa consolidated specimen was compared with that of the intact specimen to investigate the consolidation effect (Fig. 5a and b; blue spots represent pores). The porosity decreased by 41.23% (Fig. 5c) due to consolidation. The equivalent diameter of pores (d_{pore}) in the intact specimen was 0.04–0.16 mm. The frequency of $d_{pore} \geq 0.08$ mm decreased, and $d_{pore} \leq 0.08$ mm became dominant at P_c = 15 MPa (Fig. 5d). Pores with a smaller aspect ratio increased at P_c = 15 MPa (Fig. 5e), but pores with a small

angle to the horizontal flow layer remained dominant in the 15-MPa consolidated specimen (Fig. 5f).

In the X-ray CT images at P_c = 1 MPa, a rupture plane was observed in the X−Z plane of the specimen after axial compression (Fig. 6a). However, macroscopic fractures were not observed for the P_c = 15 MPa case (Fig. 6b).

An analysis of the pores around the rupture plane was performed using the blue resin-impregnated thin-section images of the specimens after axial compression at P_c = 1 MPa. The porosity near the rupture plane increased by 16.99%, and was greater than that far from the rupture plane (Fig. 6f). The frequency value of d_{pore} = 0.10 mm increased near the rupture plane (Fig. 6g), and the frequency value of d_{pore} = 0.06 mm was dominant far from the rupture plane. The frequency of a pore aspect ratio of around 0.5 decreased near the rupture plane (Fig. 6h).

4. Results of the Kimachi sandstone

4.1 Deformation and permeability

This rock exhibited brittle behavior under low confining pressure (1–7 MPa) (Fig. 7a). The magnitude of the stress drop due to failure decreased at P_c = 9–11 MPa, and almost perfect plastic behavior was observed at P_c = 13–15 MPa (Fig. 7a). The peak and residual strength increased (Fig. 7b) and Poisson's ratio decreased with increasing confining pressure, but no clear relationship was observed for the tangent modulus (Fig. 7c).

The permeability at $P_c \geq 7$ MPa after 24 h of consolidation was slightly lower than that at $P_c \leq 5$ MPa (Fig. 8a). The permeability began to decrease in the initial stage of the axial compression and reached a minimum before the peak stress, but it then began to increase and reached an almost stable value at the residual strength state (Fig. 7a). The minimum value of the permeability at P_c = 7 MPa was less than that at $P_c \leq 5$ MPa (Fig. 8b). After compression, the permeability decreased with increasing confining pressure (Fig. 8c).

By expressing the decrease ratio of permeability K_{change} from consolidation (K_{con}) to minima (K_{min}) by the equation

$$K_{change} = \frac{K_{min} - K_{con}}{K_{con}} \times 100 , \tag{18}$$

it was found that K_{change} decreased with increasing confining pressure (Fig. 8d). In addition, the permeability increased from consolidation to the post-compression

state (see Eq. 16) at P_c = 1 MPa, had almost the same values at P_c = 5–9 MPa, and decreased at P_c = 10–15 MPa (Fig. 8e).

The effect of confining pressure on the minimum and stable permeability values with respect to axial strain was evaluated by the following equations (Fig. 9):

$$\log K_{\min} = -17.41 - 0.57 \log P_c \tag{19}$$

$$\varepsilon_{\min} = 0.16 + 0.03 P_c \tag{20}$$

$$\log K_{\text{stable}} = -16.97 - 0.75 \log P_c \tag{21}$$

$$\varepsilon_{\text{stable}} = 0.81 + 0.05 P_c \quad , \tag{22}$$

where K is in m^2, P_c is in MPa, and ε is in %.

The specimen diameter decreased due to confining pressure, but recovered under axial compression to its value under atmospheric pressure at σ_L (Fig. 10a). The permeability became lowest around this point, but began to increase afterward. A similar phenomenon for residual strength was reported by Fujii et al. [19], which was confirmed and is almost the same as that for σ_L (Fig. 10b).

4.2 Micro- and macrostructures

From the blue resin-impregnated thin-section analysis, the 0.39-mm average thickness of cementing materials in the case of consolidation at 1 MPa was much thicker than the 0.25-mm average at 15 MPa (Fig. 11).

From the CT observations, a distinct main rupture plane was observed in the X−Z plane of the specimen after axial compression at P_c = 1 MPa (Fig. 12a and d). Several subrupture planes were discovered in the Y−Z and X−Y planes (Fig. 12b). The thickness of cementing materials was 0.27 mm. At P_c = 7 MPa, only one main rupture plane was found in the X−Z and Y−Z planes (Fig. 12b). At P_c = 15 MPa, no macroscopic rupture planes were observed in either the CT images (Fig. 12c) or the blue resin-impregnated thin section (Fig. 12e). The thickness of the cementing materials was 0.20 mm.

5. Results of the Inada granite

5.1 Deformation and permeability

This rock exhibited brittle failure for all of the confining pressure values considered (Fig. 13a). The peak and residual strength increased slightly with the

confining pressure (Fig. 13b). The tangent modulus and Poisson's ratio seemed to decrease slightly (Fig. 13c), but no clear relationship was observed. The reason for the lack of a clear relationship between the mechanical properties and confining pressure was the relatively low confining pressure values compared to the strength of the rock.

After 24 h of consolidation, the permeability at $P_c \geq 5$ MPa was slightly lower than it was at $P_c \leq 3$ MPa (Fig. 8a). The permeability began to decrease at the initial stage of axial loading, and reached a minimum before the peak stress. The permeability then began to increase and reached an almost stable value at the residual strength state (Fig. 13a). This tendency was the same as that observed in the case of the Kimachi sandstone.

The minimum value at $P_c = 3$ MPa was less than it was at $P_c \leq 3$ MPa (Fig. 8b). The minimum permeability after compression did not follow the axial strain–confining pressure relationship observed for the Kimachi sandstone. The relationship between the minimum permeability value (K_{min}) and confining pressure (P_c) (Fig. 9c) was clearly described by the following equation:

$$\log K_{min} = -18.04 - 1.55 \log P_c \tag{21}$$

The permeability was greater after compression than it was after consolidation, but the increase ratio decreased with increasing confining pressure up to $P_c = 9$ MPa. The ratio began to increase again at $P_c = 11–15$ MPa (Fig. 8f). The permeability was lowest when the lateral strain was around zero (Fig. 10), as was observed for the Kimachi sandstone. The residual strength was almost the same as σ_L (Fig. 10b), as stated by Fujii et al. [20].

5.2 Micro- and macrostructures

No consolidation effect was observed from the blue resin-impregnated thin-section analysis of the granite (Fig. 11b).

From the CT observations, a main rupture plane in the X−Z plane, with subrupture planes in the Y−Z plane, was observed at $P_c = 1$ MPa (Fig. 14a). The main rupture plane consisted of a network of microcracks (Fig. 14d). Numerous axial cracks from biotite grains were also observed. As described in detail by Nishiyama et al. [21], this type of microcracking was induced because biotite is softer than quartz or plagioclase. The distinct single rupture plane in the CT image (Fig. 14b) was also observed in the thin section at $P_c = 9$ MPa (Fig. 14e). This

rupture plane also consisted of a network of microcracks; however, it had a smaller width than that at P_c = 1 MPa, and axial cracks from biotite were not observed. Multiple rupture planes were observed at P_c = 15 MPa (Fig. 14c).

6. Discussion

For consolidation under a confining pressure of 15 MPa, the permeability was the lowest in the Shikotsu welded tuff. This occurred because the confining pressure was close to the unconfined compressive strength (UCS) and was sufficiently high to cause pore collapse (Fig. 5) [22]. As observed by the decrease in yield stress, pore collapse occurred during axial compression at even lower confining pressures and caused the permeability to decrease (Fig. 6). A decrease in the permeability under axial compression was also reported by Azeemuddin et al. [23] for Indiana limestone, but the confining pressure effect has not been considered in the literature. At a confining pressure of 1 MPa, the permeability did not decrease significantly in the residual strength state because of rupture plane formation. In the residual strength state, the rupture plane and the higher-porosity rock matrix near the plane (Fig. 6) were responsible for the relatively high and relatively stable permeability (Fig. 3a).

A decrease in the permeability due to consolidation was also observed in both the sandstone and granite. The main reason for the decrease in the sandstone was compaction of the grains because the cementing materials became thinner at P_c = 15 MPa (Fig. 11a). The reason for the decrease in the granite was elastic closure of microcracks; however, this was not observed in the thin sections because they were prepared after unloading (Fig. 11b).

In the sandstone and granite, the permeability decreased at the initial stage of axial compression, increased after this stage, and finally reached an almost stable value in the residual strength state. Other researchers [23-27] have also described this behavior under axial compression, but the confining pressure effect on the minimum permeability and the permeability in the residual strength state were not considered. The decrease in permeability (Figs. 7a and 13a) was due to closure of microcracks under compression, as described by Batzle et al. [28]. In particular, the closure of inclined microcracks significantly affects permeability. The increase in permeability after the initial stage of axial compression (Figs. 7a and 13a) occurred because of the nucleation, growth, and coalescence of microcracks.

This property under compression was described by Kranz [29]. The permeability increase began when the lateral strain started to exceed its value corresponding to the atmospheric pressure (Fig. 10). The increase in permeability around the peak load was due to the linking of locally dense microcracks. This characteristic under compression was also described by Kranz [29].

The permeability became stable in the residual strength state (Figs. 7a and 13a). The stable permeability was attained at a certain axial strain, which depended on the confining pressure for sandstone but not for granite (Fig. 9). Several rupture planes appeared under low confining pressures for sandstone and granite, and this was the reason for the increase in permeability following axial compression (Figs. 12a and 14a). At a confining pressure of 5–7 MPa for the Kimachi sandstone (Fig. 12b) or 7 MPa for the Inada granite (Fig. 14b), only a single rupture plane formed, causing the lower post-axial compression permeability. The disappearance of microcracks from biotite is another reason for the permeability decrease in the Inada granite.

Almost perfectly elasto-plastic deformation was observed in the Kimachi sandstone under high confining pressure (Fig.7a), and no rupture plane was present (Fig. 12). This occurred because large plastic deformation took place in the cementing materials. Conversely, in the Inada granite, subrupture planes occurred under high confining pressures (≥ 12 MPa), as was the case at a confining pressure of 1 MPa (Fig.14a and c). Thus, the permeability after axial compression again increased. The subrupture planes formed because there were no soft cementing materials between mineral grains, so a large amount of plastic deformation could not occur. Significant stress concentration occurred on the stiff and rough main rupture plane under these high confining pressures.

7. Conclusions

To clarify the effect of confining pressure on the permeability behavior of various types of rock under triaxial compression, the permeability was measured in Shikotsu welded tuff, Kimachi sandstone, and Inada granite at confining pressures of 1−15 MPa.

For the Shikotsu welded tuff, the permeability monotonously decreased with axial compression. The decrease ratio increased with confining pressure; the main

cause of the decease was attributed to pore collapse. A new equation representing the permeability as a function of confining pressure was proposed.

For the Kimachi sandstone, the permeability first decreased with increasing axial stress, but then began to increase when the total lateral strain recovered its value before the application of confining pressure, and finally showed an almost constant value in the post-peak region. The minimum and final permeability decreased with confining pressure. Compared to the permeability before axial compression, the final permeability became larger under small confining pressure but smaller under high confining pressure. The main cause of the decrease was attributed to either compaction or large plastic deformation of clay cementing materials. Equations representing the minimum and stable permeability and the strain values at the minimum point and at the beginning of stable permeability as functions of confining pressure were proposed.

For the Inada granite, the permeability behavior during axial compression was almost the same as that for the Kimachi sandstone. An equation representing the minimum permeability as a function of confining pressure was proposed. The main cause of the decrease caused by consolidation was attributed to elastic deformation. Compared to the permeability before compression, the final permeability was larger, and it decreased with smaller confining pressures. The main causes of the decrease were attributed to a decrease in the number and width of rupture planes and a decrease in the axial cracks from biotite; however, the permeability increased under larger confining pressures because of the formation of subrupture planes due to high stress concentration at the rough and stiff rupture plane.

The equations, if made more sophisticated through accumulation of additional data, could be useful for achieving more reasonable and precise HM analyses of underground caverns in various numerical simulations, such as by finite element modeling (FEM), although the authors recognize that the rupture planes in a rock specimen are different from the natural fractures or joints in a rock mass, and that further considerations are required. The finding that the decreased permeability began to increase again when the lateral strain recovered its value before the application of confining pressure could also help to formulate the permeability more precisely in terms of strain in the future.

From the experimental results, it can be stated that continuous sealability improvement can be expected in EdZs and EDZs for rocks similar to the Shikotsu welded tuff. In the case of rocks similar to the Kimachi sandstone, sealability improvement can be expected in EdZs at all confining pressures and in EDZs under relatively high confining pressure. In rocks similar to the Inada granite, sealability improvement can be expected in EdZs under all confining pressures, as was the case for the other rocks, but improvement cannot be expected in EDZs.

The temperature effect is important for performance assessments of radioactive waste repositories, which require long-term monitoring even after closure [7, 30, 31]. The authors have already completed similar experiments at 353 K, and these results will be published in the near future. The results shown here, along with those at 353 K, could contribute to reasonable designs of various types of underground caverns.

Acknowledgement

This work was partially supported by KAKENHI (22560804). We are grateful to Professor Katsuhiko Kaneko, Laboratory of Terrestrial Engineering, Hokkaido University, who kindly allowed us to use the micro-focus X-ray CT scanner.

References

[1] Borgesson L, Pusch R, Fedriksson A, Hokmark H, Karnland O, Sanden S. Final report of the zones disturbed by blasting and stress release. Swedish Nuclear Fuel and Waste Management Co (SKB), Stockholm, Stripa Proj Tech Rep; 1992. p. 8−92.

[2] Olsson O. Site characterization and validation−final report: Stripa Project. Swedish Nuclear Fuel Waste Management Co, Stockholm, Rep TR; 1992. p. 22−92.

[3] Emsley S, Olsson O, Stenberg L, Alheid H−J, Fall S. ZEDEX− a study of damage and disturbance from tunnel excavation by blasting and tunnel boring. Swedish Nuclear Fuel WasteManagement Co (SKB), Stockholm, Tech Rep; 1997. p. 30−97.

[4] Sugihara K, Matsu H, Sato T. In situ experiments on rock stress conditions and excavation disturbance in JNC's geoscientific research program in Japan. Proceedings of International Workshop Rock Mechanics of Nuclear Waste Repositories, 5−6 June, Veil, Colorado; 1999. p. 159−183.

[5] Backblom G, Martin CD. Recent experiments in hard rock to study the excavation response: Implication of the performance of a nuclear waste geological repository. Tunnel Underground Space Tech 1999;14:377−394.

[6] Sato T, Kikuchi T, Sugihara K. In−situ experiments on an excavation disturbed zone induced by mechanical excavation in neogene sedimentary rock at Tono mine, central Japan. Eng Geol 2005;6:97−108.

[7] Kwon S, Cho WJ. The influence of an excavation damaged zone on the thermal−mechanical and hydro−mechanical behaviors of an underground excavation. Eng Geol 2008;101:110−123.

[8] Fujii Y, Ishijima Y, Ichihara Y, Kiyama T, Kumakura S, Takada M, Sugawara T, Narita T, Kodama J−I, Sawada M, Nakata E. Mechanical properties of abandoned and closed roadways in the Kushiro Coal Mine, Japan. Inter J of Rock Mech Min Sci. 2011;48:585−596.

[9] Wang J, Cook P, Trautz R, flexser S, Hu Q, Salve R, Hudson D, Conrad M, Tsang Y, Williams K, Soll W, Turin J. In−situ field testing of processes.

ANL−NBS−HS−000005 REV01. Bechtel SAIC Co, Las Vegas, Navada; 2001.

[10] Tsang C−F, Bernier F, Davies C. Geohydromechanical processes in the excavation damaged zone in crystalline rock, rock salt, and indurated and plastic clays−in the context of radioactive waste disposal. Inter J of Rock Mech Min Sci. 2005;42:109−125.

[11] Rutqvist J, Stephansson O. The role of hydromechanical coupling in fractured rock engineering. Hydrogeol J 2003;11:7−40.

[12] Neuzil CE. Hydromechanical coupling in geologic processes. Hydrogeol J 2003;11:41−83.

[13] Doi S. Petrological and petrochemical studies of welded tuff. Reports of the geological survey of hokkaido 1963;29:30−103.

[14] Dhakal G, Yoneda T, Kato M, Kaneko K. Slake durability and mineralogical properties of some pyroclastic and sedimentary rocks. Eng geol 2002;65:31−45.

[15] Lin W, Takahachi M. Anisotropy of strength and deformation of Inada granite under uniaxial tension. Chinese J of Rock Mecha and Eng 2008;27:2463−2472.

[16] Al-Wardy W, Zimmerman RW. Effective stress law for the permeability of clay-rich sandstones. J Geophys Res 2004;109(B4):B04203.

[17] Brace WF, Walsh JB, Frangos WT. Permeability of granite under high pressure. J of Geophys Res 1968;73:2225− 2236.

[18] http://scion-image.software.informer.com/ Cited 27 Dec, 2011.

[19] Fukuda D, Nara Y, Kobayashi Y, Maruyama M, Koketsu M, Hayashi D, Ogawa H, Kaneko K. Investigation of self-sealing in high-strength and ultra-low-permeability concrete in water using micro-focus X-ray CT. Cement and Concrete Research 2012;42:1494-1500.

[20] Fujii Y, Ishijima Y, Kiyama T. Confining pressure− dependency coefficient in the sample constitutive equations for brittle rock. Proc. 99 Japan−Korea Joint Symp. On Rock Engineering; 1999. p. 323−330.

[21] Nishiyama T, Chen Y, Kusuda H, Ito T, Kaneko K, Kita H, Sato T. The examination of fracturing process subjected to triaxial compression test in Inada granite. Eng Geol 2002;66:257–269.

[22] Zaman M, Roegiers J-C, Abdulraheem A, Azeemuddin M. Pore colppase in weakly cemented and porous rocks. J of Energy Resources Tech 1994;116:97-103.

[23] Azeemuddin M, Roegiers J−C, Suir P, Zaman M, Kukreti AR. Stress−dependent permeability measurement of rocks in a triaxial cell. In: Tillerson JR, Wawersik WR, editors. Proceedings of the 35th US Symposium on Rock Mechanics; 1995. p. 645–650.

[24] Morita N, Gray KE, Fariz AA Srouji, Jogi PN. Rock−property changes during reservoir compaction. SPE Formation Evaluation; 992. p. 197−205.

[25] Zhu W, Wong T−F. The transition from brittle faulting to cataclastic flow: permeability evolution. J Geophys Res 997; 102(B1):3027−3041.

[26] Heiland J. Laboratory testing of coupled hydro−mechanical processes during rock deformation. Hydrogeol J 2003; 11:122−141.

[27] Keaney GMJ, Meredith PG, Murrel SAF. Laboratory study of permeability evolution in a tight sandstone under nonhydrostatic stress conditions. Eurock 96; 1998. p. 329−335.

[28] Batzle ML, Simons G, Siegfried RW. Microcrack closure in rocks under stress: Direct observation. J of Geophys Res 1980;85:7072−7090.

[29] Kranz RL. Microcracks in rocks:A review. Tectonophysics 1983;100:449−480.

[30] Hudson JA, Stephansson O, Anderson J. Guidance on numerical modeling of thermo−hydro−mechanical coupled processes for performance assessment of radio active waste repositories, Inter J of Rock Mech Min Sci. 2005;42, 850−870.

[31] Rutqvist J, Barr D, Datta R, Gens A, Millard A, Olivella S, Tsang C−F, Tsang Y. Coupled thermal−hydrological−mechanical analysis of the Yucca Mountain Drift Scale Test− Comparison of field measurements to predictions of four different numerical models, Inter J of Rock Mech Min Sci. 2005;42, 680−697.

Table 1: Physical properties of the rocks shown as "average value (number of specimen) ± standard deviation". UCS: Uniaxial Compressive Strength.

Name of rock	V_p of specimen (km/s)	V_s of specimen (km/s)	Dry density (g/cm^3)	Effective porosity (%)	UCS (saturated) (MPa)
Shikotsu welded tuff	1.745 (2) ± 0.007	1.245(2) ± 0.021	1.304 (10) ± 0.012	36.5 (10) ± 2.3	13.53 (2) ± 2.74
Kimachi sandstone	2.24(13) ± 0.08	1.478 (13) ± 0.039	1.981(13) ± 0.01	18.54(13) ± 0.95	20.5 (2) ±2.4
Inada granite	2.87 (17) ± 0.07	2.09 (17) ± 0.06	2.70 (17) ± 0.01	0.584 (17) ± 0.023	180.9 (2) ±16.9

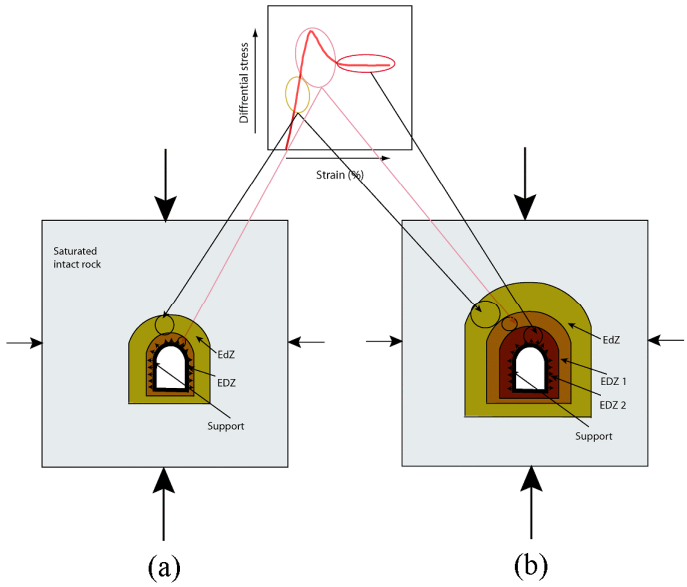

Fig. 1. Schematic diagram of an underground opening. (a) Initial state, (b) after rock around the excavation reached the residual strength state.

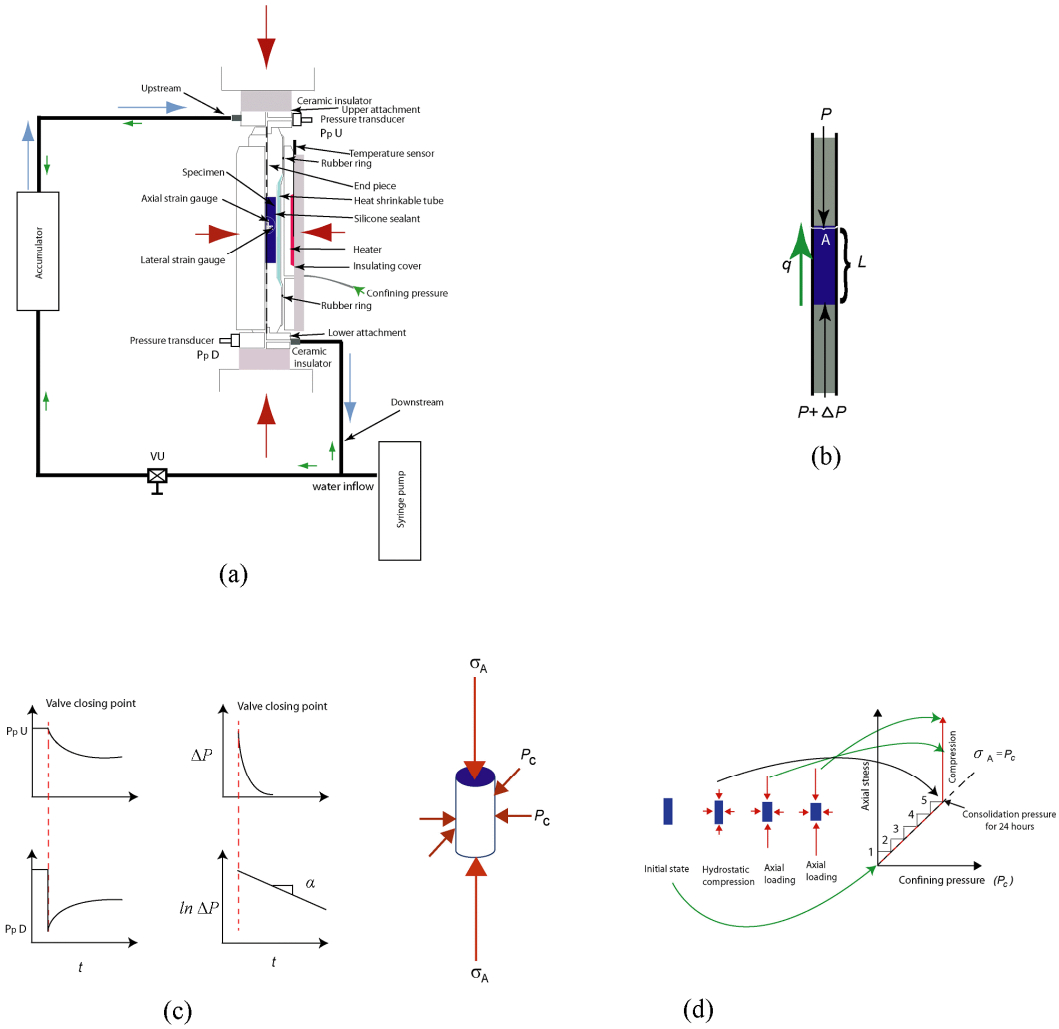

Fig. 2. Experimental setup and procedure. (a) Experimental setup for the transient pulse method. (b) Schematic diagram for permeability measurement using the constant flow method. (c) Schematic diagram for permeability measurement using the transient pulse method. (d) Schematic diagram showing the steps for reaching the desired confining pressure and compression.

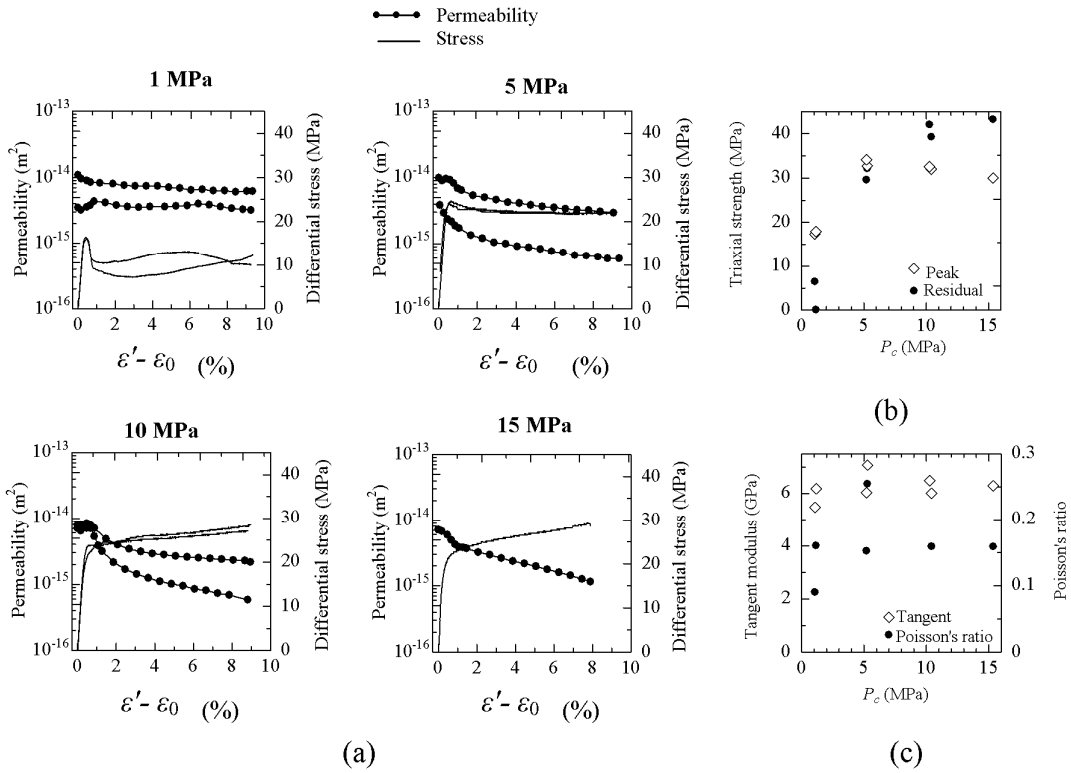

Fig. 3. Stress-strain, permeability relationship and mechanical properties of Shikotsu welded tuff. (a) Stress, axial strain and permeability relationship. (b) Peak or yield differential stress, residual strength with confining pressure. (c) Tangent modulus and Poisson's with confining pressure.

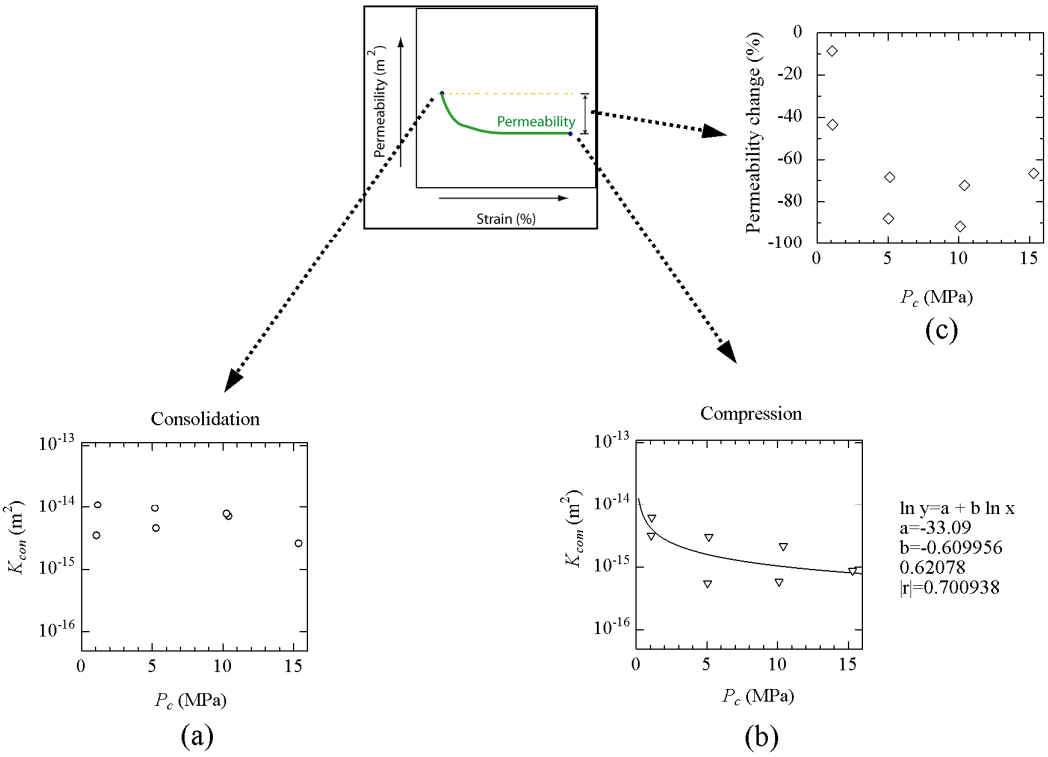

Fig. 4. Confining pressure effect on the permeability change of the Shikotsu welded tuff. Permeability after (a) consolidation and (b) axial compression. (c) Decrease of permeability.

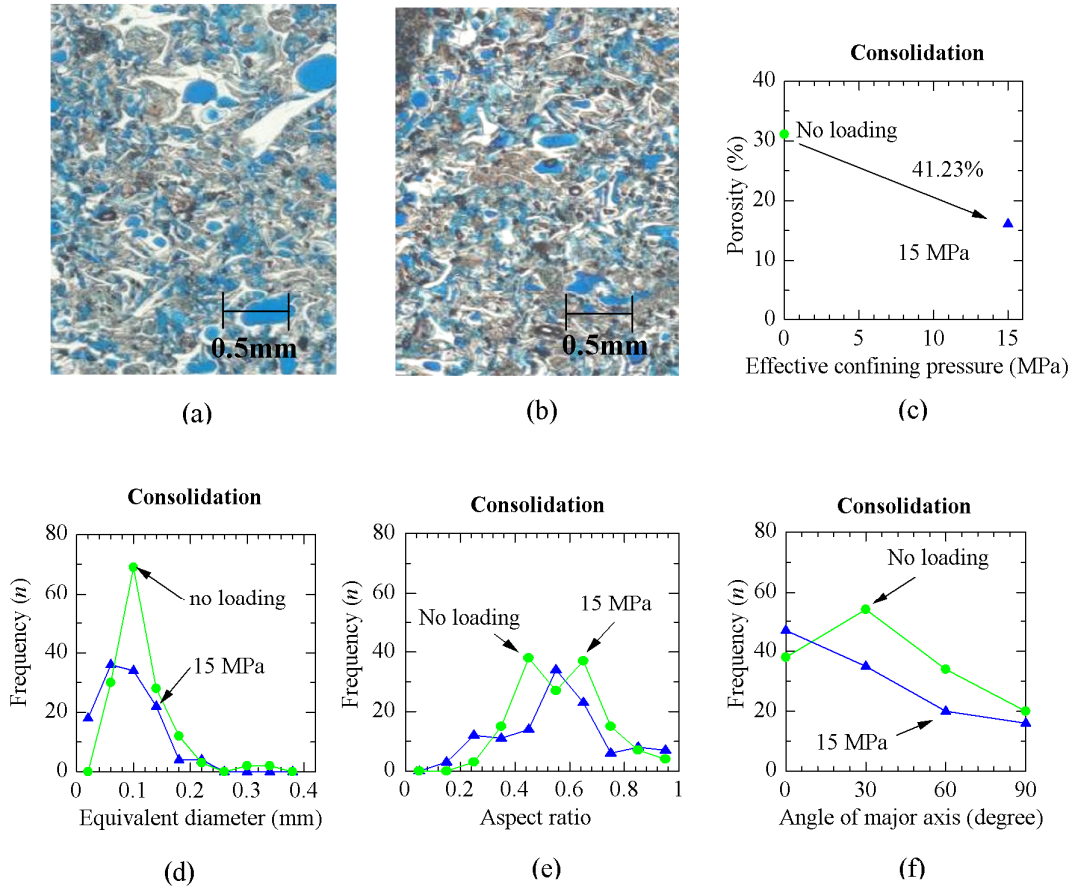

Fig. 5. Blue resin-impregnated thin-section images and analyses of the fresh and consolidated specimens of Shikotsu welded tuff. The blue spots represent pores in the rock. (a) Image of the intact specimen. (b) Image after consolidation at 15 MPa. (c) Porosity. (d) Equivalent diameter. (e) Aspect ratio. (f) Angle of major axis to the horizontal flow layer.

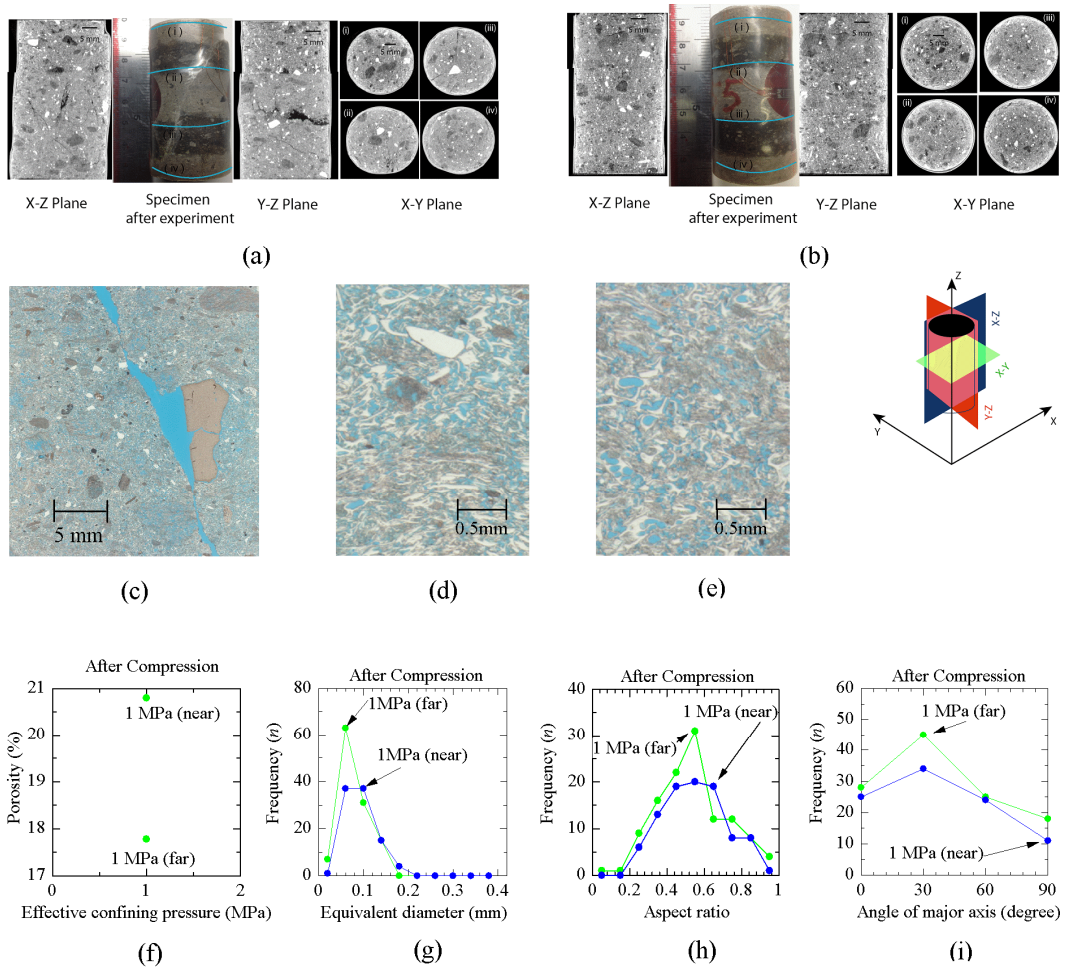

Fig. 6. Specimen, CT images, blue resin-impregnated thin-section images, and analyses after axial compression of Shikotsu welded tuff. Specimen and CT images at (a) 1 MPa and (b) 15 MPa. (c) Image at 1 MPa. Image at 1 MPa (d) near the shear plane and (e) far from the shear plane. (f) Porosity near and far from the rupture plane. (g) Equivalent diameter. (h) Aspect ratio. (i) Angle of major axis to the flow layer (horizontal). The loading direction is vertical.

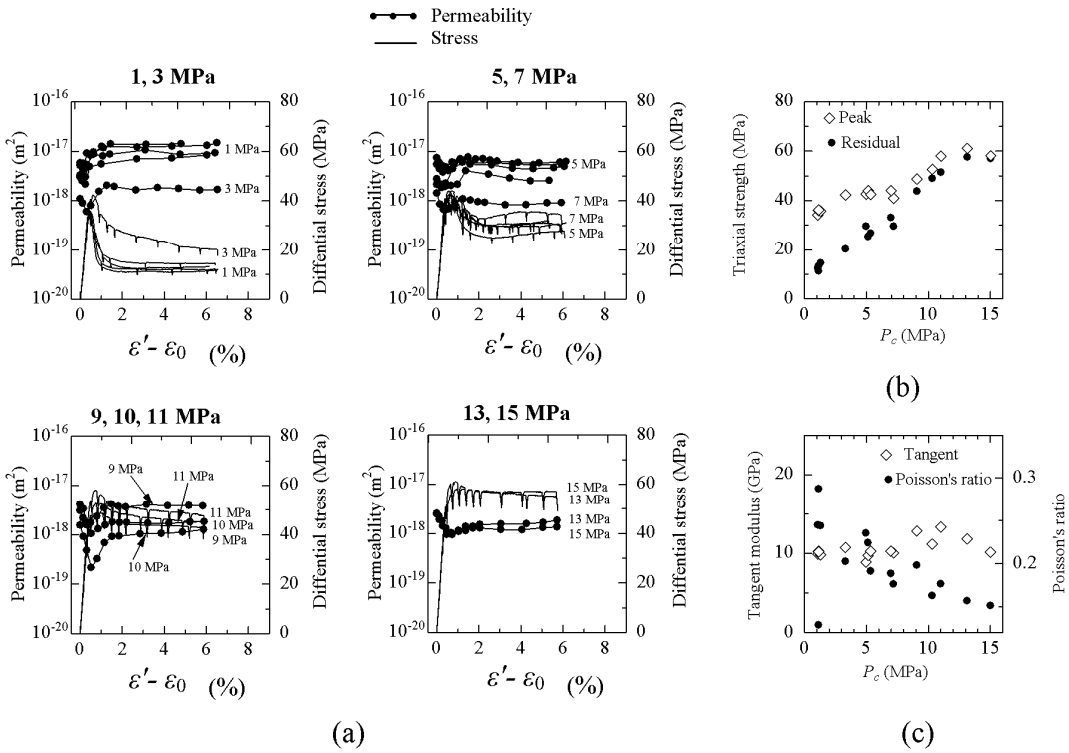

Fig. 7. Stress-strain, permeability relationship and mechanical properties of Kimachi sandstone. (a) Stress, axial strain and permeability relationship. (b) Peak differential stress, residual strength with confining pressure. (c) Tangent modulus and Poisson's ratio with confining pressure.

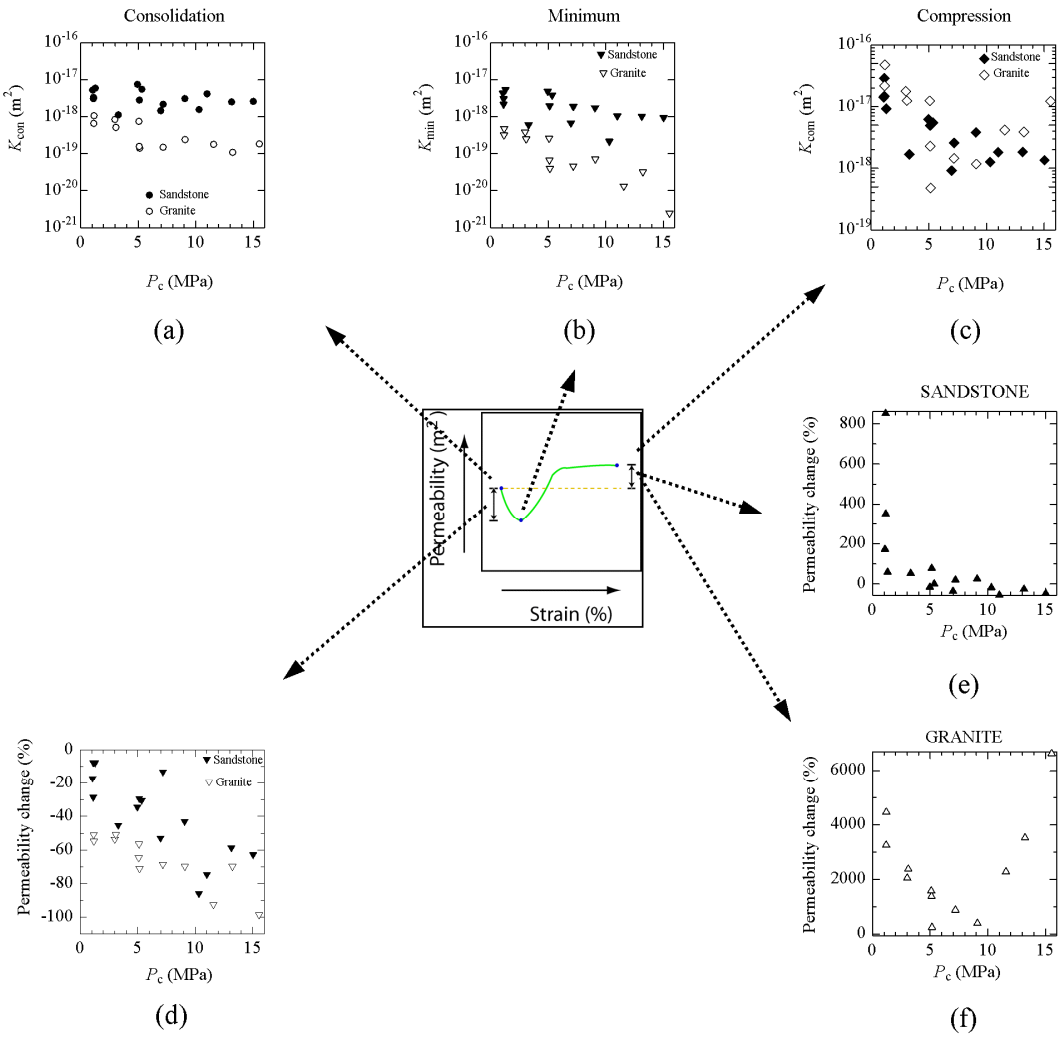

Fig. 8. Confining pressure effect on the permeability change of Kimachi sandstone and Inada granite. (a) Permeability after consolidation. (b) Minimum permeability. (c) Permeability after axial compression. (d) Permeability decrease from consolidation to the minimum value. (e) Permeability change from consolidation to post-compression.

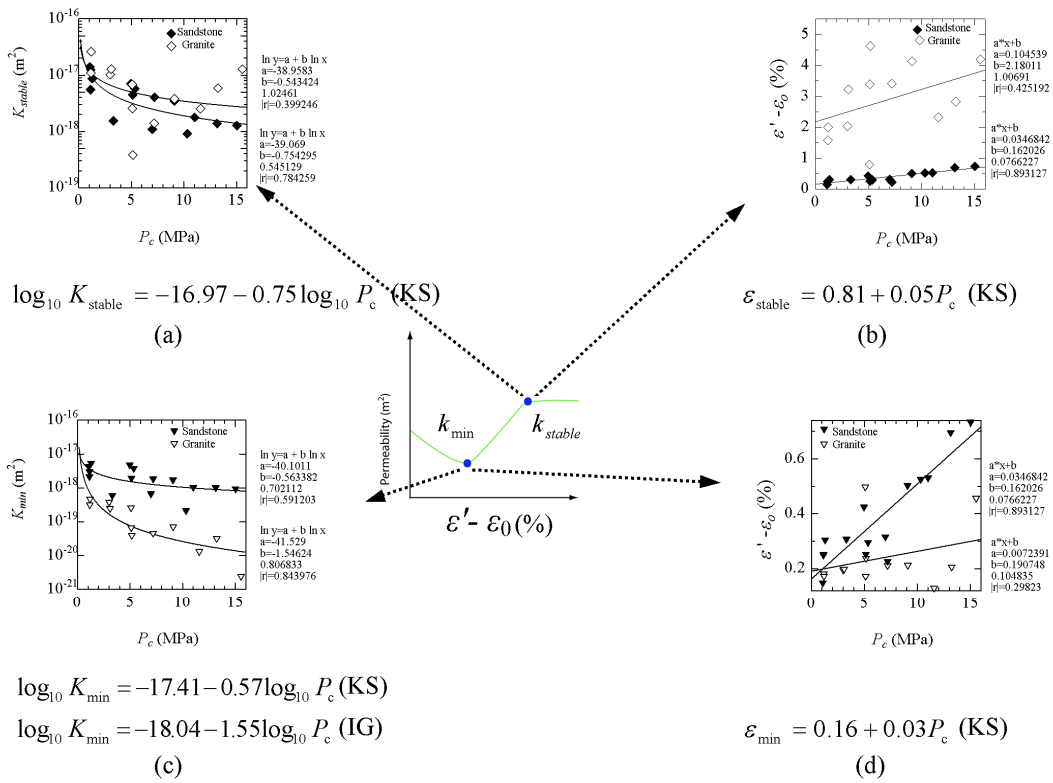

Fig. 9. Confining pressure dependency of minimum and stable permeability in relation to axial stain for Kimachi sandstone (KS) and Inada granite (IG). (a) Stable permeability and confining pressure. (b) Axial strain at stable permeability and confining pressure. (c) Minimum permeability and confining pressure. (d) Axial strain at minimum permeability and confining pressure.

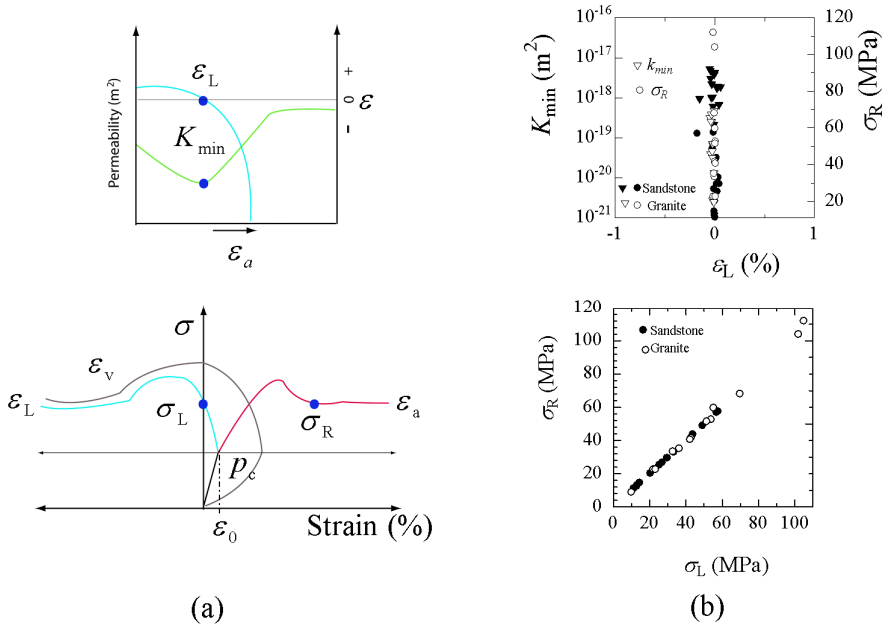

Fig. 10. Relationship between permeability, lateral strain, residual strength, and stress at zero lateral strain. (a) Schematic diagram showing the point of lateral strain at minimum permeability (ε_L, K_{min}) and σ_L; σ_R is the stress at the lateral strain of residual strength. (b) The experimental results of the ε_L, K_{min} and σ_L, σ_R.

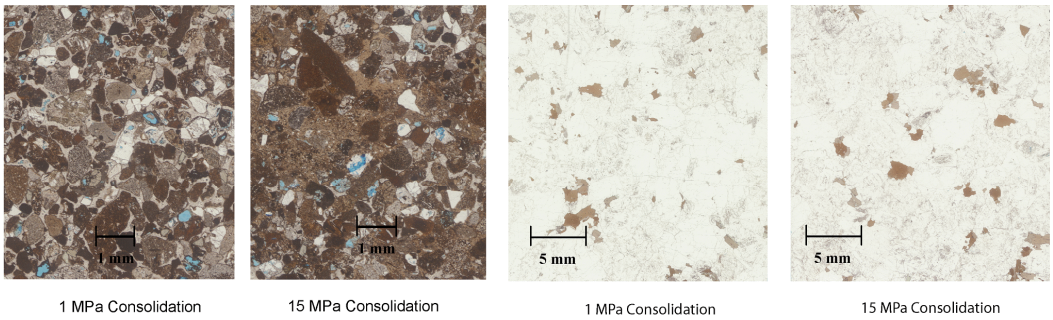

(a) (b)

Fig. 11. Blue resin-impregnated thin-section images of the specimen after consolidation. (a) Kimachi sandstone. (b) Inada granite.

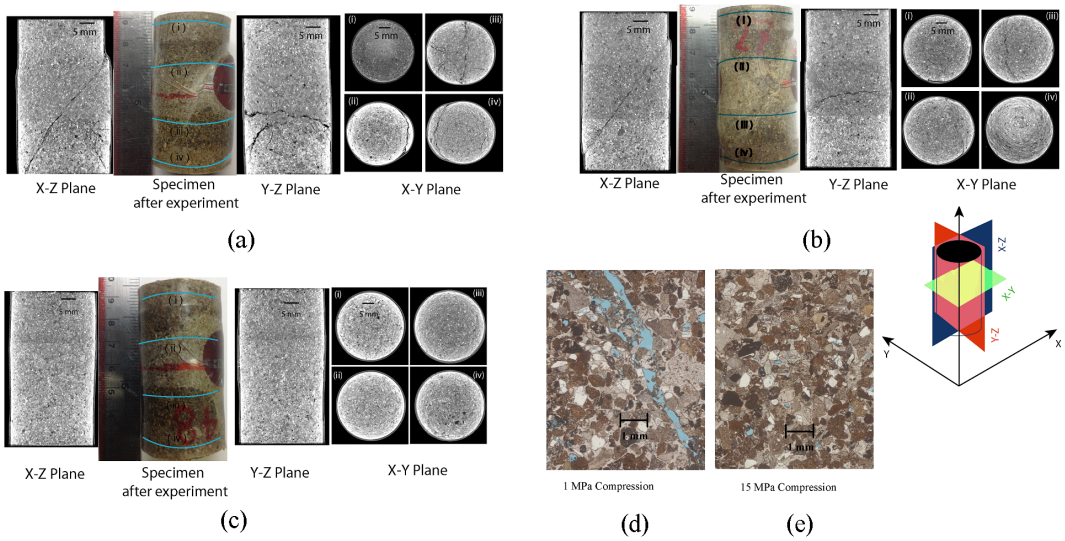

Fig. 12. Specimen, CT images, and blue resin-impregnated thin-section images of the specimens after axial compression of Kimachi sandstone. Specimen and CT images at (a) 1 MPa, (b) 7 MPa, and (c) 15 MPa. Blue resin-impregnated thin-section image at (d) 1 MPa and (e) 15 MPa. The loading direction is vertical.

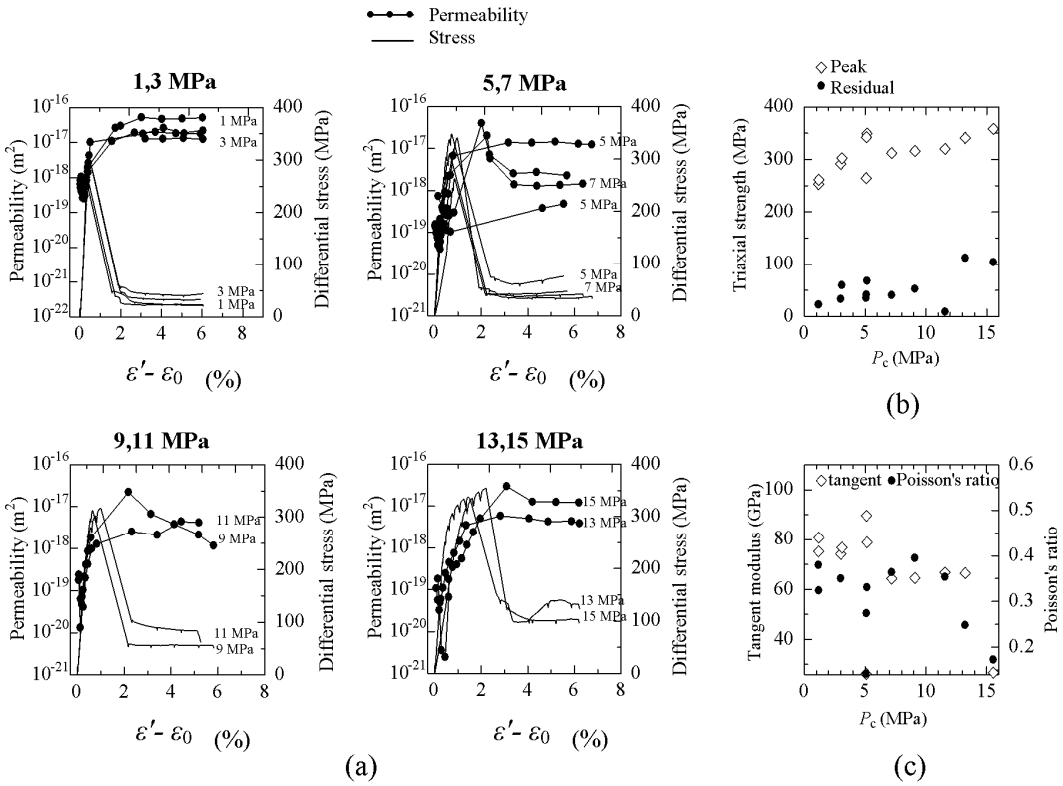

Fig. 13. Stress Stress-strain, permeability relationship and mechanical properties of Inada granite. (a) Stress, axial strain and permeability relationship (b) Peak differential stress, residual strength with confining pressure. (c) Tangent modulus and Poisson's ratio with confining pressure.

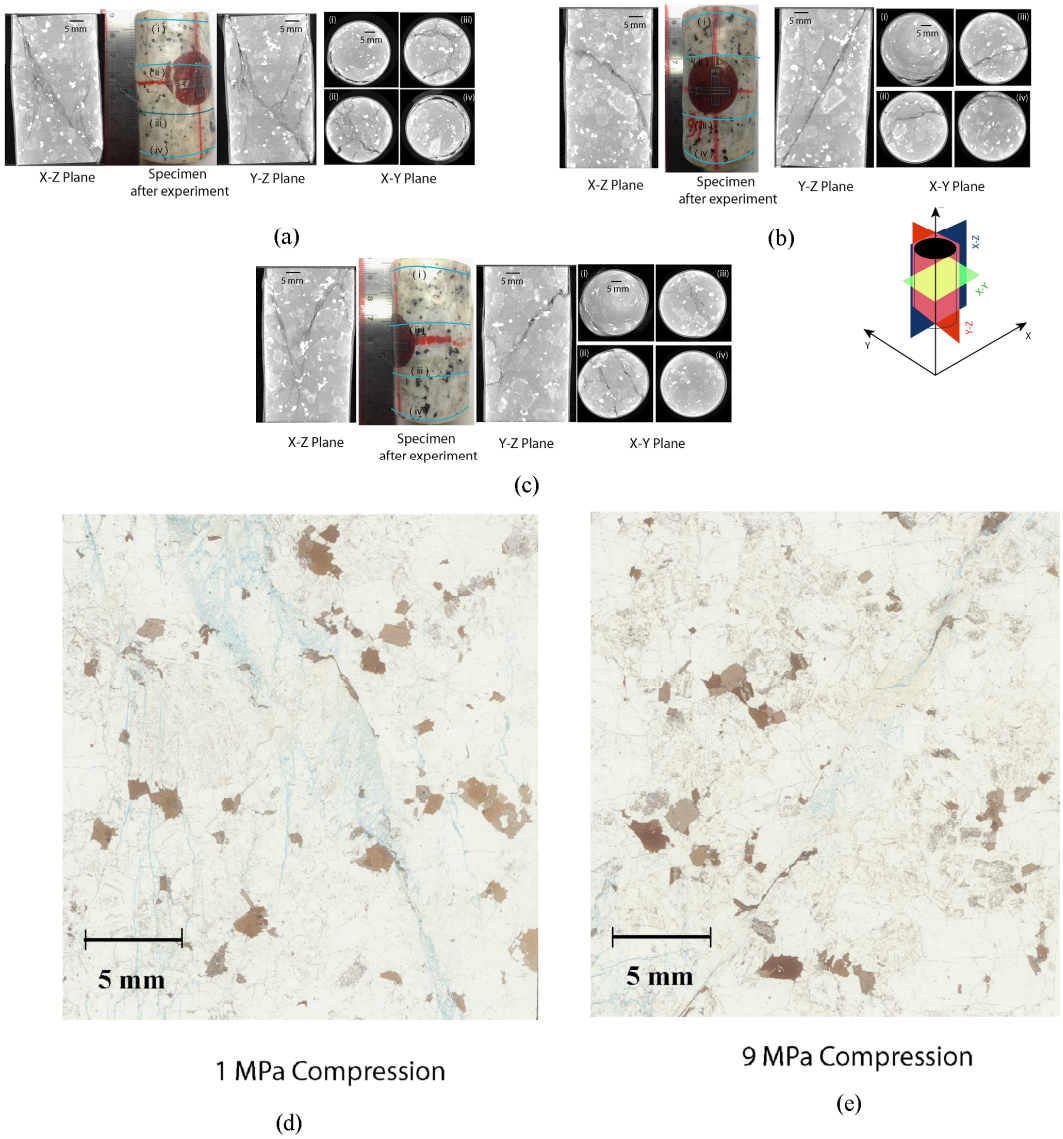

Fig. 14. Specimen, CT images, and blue resin-impregnated thin-section images of the specimens after axial compression of Inada granite. Specimen and CT images at (a) 1 MPa, (b) 7 MPa, and (c) 15 MPa. Blue resin-impregnated thin-section image at (d) 1 MPa and (e) 9 MPa. The loading direction is vertical.